Article

Gas-Sensing Properties of Graphene Functionalized with Ternary Cu-Mn Oxides for E-Nose Applications

Margus Kodu *, Rainer Pärna, Tea Avarmaa, Indrek Renge, Jekaterina Kozlova, Tauno Kahro ⓘ **and Raivo Jaaniso** ⓘ

Institute of Physics, University of Tartu, W. Ostwaldi 1, 50411 Tartu, Estonia
* Correspondence: margus.kodu@ut.ee

Abstract: Chemiresistive gas sensors were produced by functionalizing graphene with a ~3 nm layer of mixed oxide xCu$_2$O·yMnO using pulsed laser deposition (PLD) from a hopcalite CuMn$_2$O$_4$ target. Sensor response time traces were recorded for strongly oxidizing (NO$_2$, O$_3$) and reducing (NH$_3$, H$_2$S) poisonous gases at ppb and ppm levels, respectively. The morphology of the MOX layer was modified by growth temperature during PLD, resulting in the optimization of the sensor response. Differences in decomposition or oxidation rates on catalytically active metal oxide (MOX) were utilized to achieve partial selectivity for pairs of gases that have similar adsorption and redox properties. The predominant selectivity towards ozone in most samples at different measuring conditions remained difficult to suppress. A distinct selectivity for H$_2$S emerged at higher measurement temperatures (100–150 °C), which was assigned to catalytic oxidation with O$_2$. Several gas–MOX interaction mechanisms were advanced to tentatively explain the sensor behavior, including reversible electron transfer in the simplest case of NO$_2$, decomposition via ionic transients for O$_3$, and complex catalytic oxidative transformations for NH$_3$ and H$_2$S.

Keywords: ammonia; catalysis; chemiresistive sensor; gas sensor; graphene; hopcalite; metal oxide; ozone; NO$_2$; H$_2$S

1. Introduction

The very high electron mobility in graphene (Gr), in conjunction with the low concentration of charge carriers at the Dirac point, renders its conductance highly responsive to perturbations on the Gr surface [1,2]. In a real atmosphere containing chemically reactive principal components O$_2$ and H$_2$O, in addition to extremely variable and complex mixture of gases, vapors, and aerosols, the Gr sensors tend to suffer poisoning, i.e., a gradual loss of sensitivity and reversibility of response. Small analyte molecules with a high electron affinity, such as NO$_2$ and O$_3$, or a low ionization energy, such as NH$_3$, seem not to stick to Gr for long enough for a chemisorption act (i.e., electron transfer from/to Gr) to take place, because of insufficient physical adsorption energy ($\leq$50 meV) [3]. Substitution of carbon with heteroatoms [4], partial damage of the Gr lattice by reactive oxygen ion etching [5], or even ozone [6] could impact Gr gas sensitivity. The direct functionalization of Gr, involving the conversion of the sp^2 C atom into a tetrahedral sp^3 state, is clearly not favorable because of the local destruction of π-electronic conjugation in the vicinity of site designed to bind the analyte molecule. (Point) defects, dopants, or substituents in Gr seem to make weak and nonselective binding sites, despite high expectations [4]. Alternatively, Gr is kept intact, thus preserving its transducer properties. Instead of destroying the Gr lattice, a thin layer of strongly adsorbing, catalytically active and highly selective material is placed upon Gr in a way that electron transfer between the phases remains possible. The latter approach was shown to be effective for small molecules, when Gr is functionalized with metal oxides (MOX) by means of pulsed laser deposition (PLD) [7–12]. The use of MOX for adsorption and catalysis yields far better results than "pristine" or "intact" Gr alone. Graphene is reserved the role of an ultimately thin electrical transducer, while the thinness of Gr as an

adsorbing substrate, where both surfaces could be exposed to the ambient environment, is actually not exploited. With the aim of minimizing the energy consumption, our first sensors were designed to operate at room temperature (RT). At RT, the recovery can be sluggish and several flammable gases (H_2, CO, CH_4) do not react at all.

In a search for suitable activators to render chemiresistive Gr sensors sensitive to CO at RT, the historically well-known CO oxidation catalyst hopcalite was selected. In the context of chemical warfare during WWI, binary oxide systems capable of promoting oxidation of CO at ambient conditions were found based on $CuMn_2O_4$, which is isomorphous to spinel $MgAl_2O_4$ structure [13–19]. The name hopcalite derives from Johns Hopkins University and the University of California, where the research was carried out. It is still in use for the respiratory protection of firefighters, miners, and scuba divers.

Besides CO oxidation at RT, mixed Cu and Mn oxides can promote the (oxidative) decomposition of O_3, NH_3, and various volatile organic compounds (VOCs). In the copper manganite spinels $Cu_xMn_{3−x}O_4$, the variable valence of $Cu^{1+/2+}$ and $Mn^{3+/4+}$ residing in tetrahedral and octahedral crystallographic sites is responsible for their versatile properties [19]. Bearing in mind that hopkalite needs a higher growth temperature (*T*) of about 900 °C, there was little hope that the spinel phase would reform upon PLD onto Gr. The film growth temperature (*T*) could only be raised up to 300 °C, when some crystal grain formation was initiated. Indeed, no RT sensor response to CO was obtained, but the same system proved effective for more reactive NH_3 and H_2S, and NO_2 and ozone.

The reducing gases NH_3 and H_2S, and the strongly oxidizing NO_2 and O_3 are highly poisonous and have devastating effects on our health. Owing to NO_2 and O_3, the air quality is poor in areas with busy traffic, while NH_3 and H_2S linger at smelly locations, such as farms, fertilized fields, sewage collection and waste treatment facilities, landfills, etc. Miniature, lightweight, and affordable sensor systems for personal use are needed to raise an alarm or inform legal action. Small gas molecules with pronounced electron acceptor properties (NO_2, O_3) can influence graphene electric conductivity at very low concentrations (down to 1 ppb), while reducing species (NH_3, H_2S) are usually somewhat less reactive (<1 ppm) [1–8]. Several nm-thick, amorphous layers of metal oxides (MOX), pulsed-laser deposited on Gr can be very potent activators, capable of providing high sensitivity and partial selectivity [7–12].

Because of their very similar redox properties and chemisorption energies, selective detection remains a challenge for the strongly electron accepting gases NO_2 and ozone (with electron affinities EA of 2.27 and 2.10 eV, respectively), or the reducing gases NH_3 and H_2S (with ionization potentials IP 10.1 and 10.5 eV) [20]. In principle, the elementary processes on MOX surfaces can be of different types. In the case of NO_2, reversible electron transfer is most plausible, since the nitrite anion is relatively stable. On the other hand, O_3 and its anion radial are prone to splitting into oxygen, which is boosted by catalysis [21,22]. Finally, reducing flammable gases will undergo catalytic oxidation on MOX surfaces, depending on the composition and structure of the surface, relative humidity (RH), and temperature. Variable interaction mechanisms with the receptor surface suggest that it may be possible to distinguish between similar gases with MOX/Gr sensors. Achieving partial selectivity was the goal of this work.

Different relative responses in an array composed of several sensors coupled with multichannel recording and treatment of signals, i.e., the electronic nose principle, can provide selectivity. The "nose" consists of many single sensors with different sensing properties that are integrated into microarrays, whereby the output signals would be further processed by a suitable machine learning algorithm to differentiate between individual gases in a complex mixture. It is possible to obtain partial selectivity of Gr sensors to various polluting gases by using distinctive functionalizing materials and deposition conditions [11]. Individual gases in mixtures can be distinguished with several Gr-based single sensors working simultaneously, while treating the output signals with a suitable machine learning algorithm [12]. Besides providing selectivity, materials that make up the sensor structure must be stable under the operating environmental conditions. In this work, single layer Gr

was functionalized by using the PLD method with a $CuMn_2O_4$ target, to deposit mixed oxides $xCu_2O \cdot yMnO$ on Gr. Sensor responses to the harmful gases NO_2, O_3, NH_3, and H_2S were studied under different conditions, keeping in mind the use in e-nose applications.

2. Experimental Section

2.1. Materials and Methods

The routine Gr transfer and PLD functionalization procedures have been described previously [7–12]. In short, chemical vapor deposited (CVD) single layer Gr was transferred onto a $10 \times 10 \times 0.5$ mm^3 Si/SiO_2 substrate carrying Ti/Au (6/100 nm) electrodes (Figure 1a). A KrF excimer laser (COMPexPro 205, Coherent Lambda Physic GmbH, Göttingen, Germany) wavelength 248 nm, pulse width ~25 ns, repetition rate 5 Hz, energy density on the target 3.0 J/cm^2) was utilized for deposition of a thin oxide layer on top of the $Si/SiO_2/Gr$ structure using ceramic $CuMn_2O_4$ as a target. The substrate was kept either at RT or 300 °C, and the buffer gas was N_2 at 0.1 mbar. The distance between substrate and target was fixed at 75 mm. Ceramic pellets of $CuMn_2O_4$ were prepared by grinding (sub)stoichiometric (1:3 to ensure the spinel phase [23]) amounts of CuO (99.7% pure, Alfa Aesar, Haverhill, MA, USA) and MnO_2 (chemically pure, Soyuzreaktiv) in an agate mortar, pressing at 500 MPa, and firing in pure O_2 flow (not air) at 1000 °C (instead of 860 °C, for better hardening) for 40 h [24].
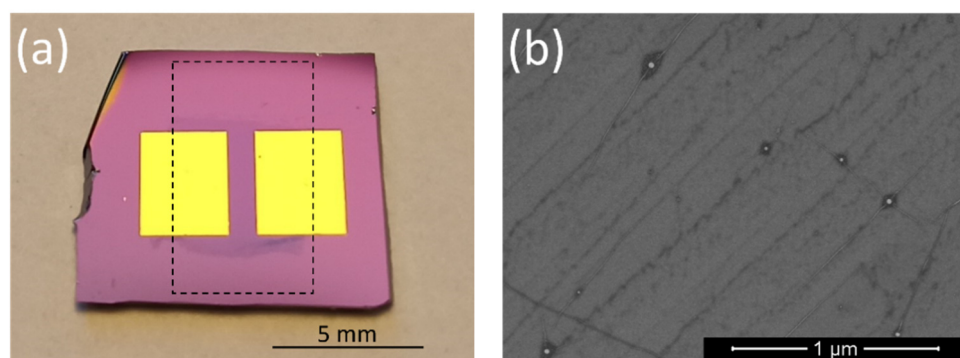

Figure 1. (**a**) Photograph of a sensor system showing the Si/SiO_2 substrate, the CVD Gr, and Au electrodes. The gap between the electrodes is 1 mm $\times$ 4 mm. The graphene sheet on top of Si/SiO_2 is barely visible due to slightly different reflection properties. The black dashed box indicates approximate PLD area; (**b**) SEM picture of pristine Gr.

The Raman spectra were recorded with a Renishaw inVia micro-Raman spectrometer (excitation wavelength 514 nm, spot size ~1 µm, incident power 1 mW).

SEM images were obtained using a FEI Helios NanoLab 600 (FEI, Hillsboro, OR, USA) electron microscope. Images were acquired using a through-the-lens detector; the electron beam acceleration voltage was 10 kV.

The X-ray photoelectron spectroscopy (XPS) and near edge X-ray absorption fine-structure spectroscopy (NEXAFS) were applied to investigate the chemical state and electronic structure of the starting material (PLD target) and deposited layers on Gr.

XPS measurements were conducted using a surface station equipped with an electron energy analyzer (SCIENTA SES 100, Scienta Scientific AB, Uppsala, Sweden) and a non-monochromatic twin anode X-ray tube (Thermo XR3E2, Thermo Fisher Scientific, Waltham, MA, USA), with characteristic energies of 1253.6 eV (Mg K$_{\alpha1,2}$, full-width at half-maximum, FWHM 0.68 eV) and 1486.6 eV (Al K$_{\alpha1,2}$, FWHM 0.83 eV). The analyzer–source angle was 45°. All XPS measurements were performed in ultrahigh vacuum (UHV) conditions. The binding energy scales in XPS experiments were referenced to a binding energy of C 1s 284.6 eV photoemission line (sp^2-graphene). Raw data were processed using the Casa XPS (version 2.3.23) [25] software. Data processing involved the removal of K$_\alpha$ and K$_\beta$ satellites and the background and fitting of components. Background removal was performed using

Shirley background; for fitting components, a Gauss–Lorentz hybrid function was used (GL70, Gauss 30%, Lorentz 70%) for the best fit.

The NEXAFS measurements were carried out on a FinEstBeAMS beamline solid state endstation at the MAX-IV synchrotron (Lund, Sweden) [26]. The NEXAFS was obtained in the total electron yield mode by measuring the sample drain current. Data processing involved the removal of the background, simultaneously measured from a gold mesh placed in front of the sample. The NEXAFS spectra were simulated by using the CTM4XAS program for EELS and XAS [27].

The measurements of electrical characteristics and gas sensitivity were performed with a Keithley 2400 source meter (Keithley Instruments, Cleveland, OH, USA,) in sample chamber with a volume of 7 cm^3, equipped with a gas mixing system, based on five mass flow controllers (model SLA5820, Brooks Instrument, Hatfield, PA, USA). The total gas flow through the chamber was kept constant at 200 sccm, and the flow rates of individual gases (N$_2$, O$_2$, NO$_2$/N$_2$ mixture, NH$_3$/N$_2$ mixture, H$_2$S/N$_2$ mixture; all 99.999% pure) were varied by mass flow controllers. Since the testing was performed in a flow-through regime, the gas pressure in the test chamber was normal atmospheric pressure. Ozone was produced with a UV-lamp-based generator, and the resulting O$_3$ concentration was continuously monitored with an analyzer (model 430, Teledyne Technologies, Thousand Oaks, CA, USA). The O$_2$ content in the gas mixture was always kept constant at 21%. Gas response was measured with synthetic air as a carrier gas with 20–50% relative humidity (RH), set by passing a predetermined part of the N$_2$ gas volume through a water bubbler. The composition of gas flow was computer-controlled with a LABVIEW-based software.

The sensor measurements were conducted either under UV light excitation at RT or at an elevated T of 100 or 150 °C (without UV). During the experiments with UV light excitation, the 365 nm light intensity from a Xe/Hg high-pressure lamp (Hamamatsu Photonics, Shizuoka, Japan) incident on the sample was ~15 mW/cm^2. The UV wavelength of 356 nm was selected with a narrow-band interference filter (Andover). The UV exposure is required, since the signal recovery at RT tends to be too slow to be of practical value.

2.2. Sensor System Characterization

The surface morphology of pristine graphene on Si/SiO$_2$ (300 nm thick) wafer substrate (Figure 1a) is shown in a scanning electron microscope (SEM) image (Figure 1b). The features appearing darker in the image are typical for transferred CVD graphene. It seems that graphene follows the uneven surface topography of polycrystalline Cu foil used in Gr synthesis. Some of the line details possibly follow the wrinkles formed during the Gr transfer. Figure 2 depicts SEM images of graphene sensor surfaces after PLD of thin (~3 nm) films of xCu$_2$O·yMnO. The thickness of the film was estimated based on our earlier data about the growth rate of oxide materials under similar deposition conditions. Deposition at the RT results in a rather uniform layer of possibly amorphous material (left panel in Figure 2), while the oxide deposited at 300 °C formed discrete grains of about ~7 nm in diameter (right panel). Previously, we deposited thin layers of oxide material with thicknesses of less than a nanometer (0.6 nm of V$_2$O$_5$) [8–11] or several nm (6.5 nm of ZrO$_2$) [7] on graphene at RT. The SEM images of these oxide layers appeared to show a similar smoothness to the xCu$_2$O·yMnO deposited at RT in this work.

In this study, the upper T limit was carefully investigated and 3D nanocrystallization was achieved at 300 °C (Figure 2), leading to damage to the Gr according to the Raman spectra (Figure 3), but this was tolerable in terms of loss of electric conductivity. With the increasing T, oxides of less reactive metals will be reduced by carbon, and Gr is no exception. At 300 °C, the surface mobility of atoms seems to be large enough to enable (crystalline) grain formation in the growing material.

The Raman spectrum of pristine CVD Gr (Figure 3), recorded in the gap between the electrodes, is characteristic of single layer CVD Gr with a low defect density. The G and 2D bands peak at 1597 ± 1 cm^{-1} and 2699 ± 1 cm^{-1} have an FWHM of 15 cm^{-1} and 33 cm^{-1}, respectively. These parameters, together with the 2D to G peak intensity ratio of

approximately one to three, correspond to a single layer Gr [28]. The very low intensity of the defect-related D peak, located at 1351 ± 1 cm^{-1}, is an indication of a low point defect density in the pristine CVD Gr samples [28,29]. The defect densities increase greatly during the PLD functionalization as a result of bombardment with high energy plasma particles [7], as indicated by the emergence of defect-related D and D' bands in the Raman spectra and a simultaneous decrease in the G and 2D bands. It follows from the comparison of the 2D and D band intensities that the resulting defect density is considerably larger for Gr functionalized at 300 °C, compared to the sample grown at RT. It is probable that the added thermal energy $k_\mathrm{B}T$ to Gr lowers the damage threshold energy caused by the impinging PLD plasma species, in particular, by means of oxidation.
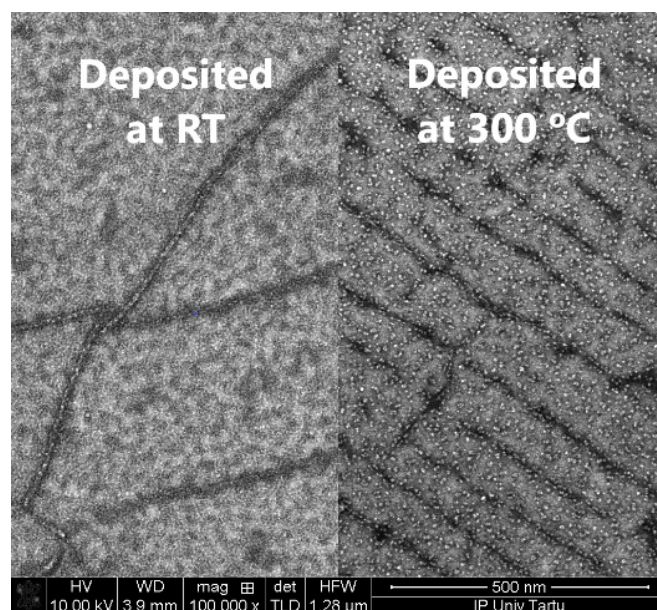

Figure 2. Scanning electron microscopy images of graphene with xCu$_2$O·yMnO layers deposited at different temperatures: 25 (**left panel**) and 300 °C (**right panel**).
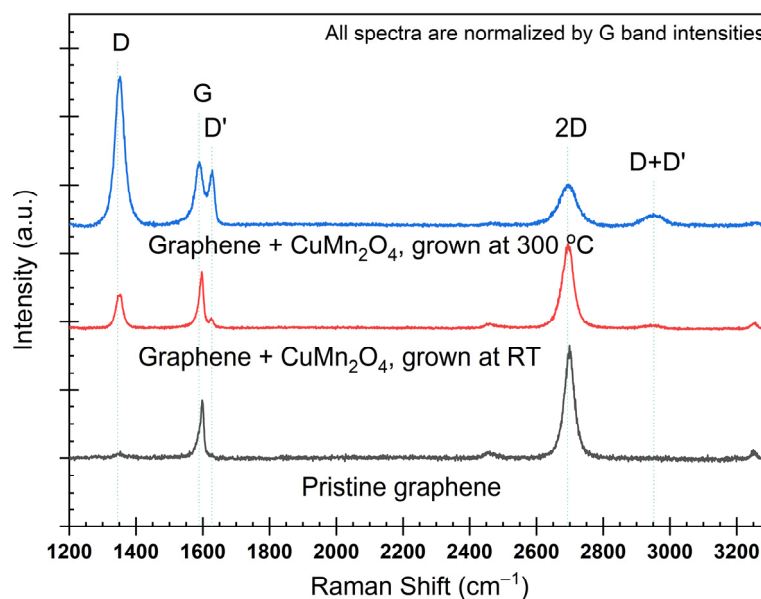

Figure 3. Raman spectra revealing differences in defect densities of pristine and functionalized graphene.

The Cu $2p_{3/2}$ photoelectron (PE) spectrum of the PLD target ($CuMn_2O_4$ target) consists of two peaks, where the PE line at a 930.7 eV binding energy (Figure 4a) is attributed to Cu^+ in $CuMn_2O_4$ [24]. The broad PE line at 933.4 eV was assigned previously to tetrahedral Cu^{2+} in $CuMn_2O_4$ [24]. The cations Cu^+ and Cu^{2+} are present in about equal amounts, Cu^+ being recognizable by an especially low-energy line peaking at ~931 eV, characteristic for spinel structure [16,24]. In the Mn L region, the near edge X-ray absorption spectroscopy (NEXAFS) contour is broad (Figure 4b, $CuMn_2O_4$ target) and very similar to the Mn_3O_4 ($MnO \cdot Mn_2O_3$) spectrum (not shown), where Mn^{3+} is located in the octahedral positions, while Mn^{2+} is in the tetrahedral positions [30]. This indicates the presence of Mn^{2+} and Mn^{3+} in comparable amounts, and some Mn^{4+} [16]. Therefore, the pressed and baked ceramic PLD target lost some oxygen and was no longer stoichiometric.
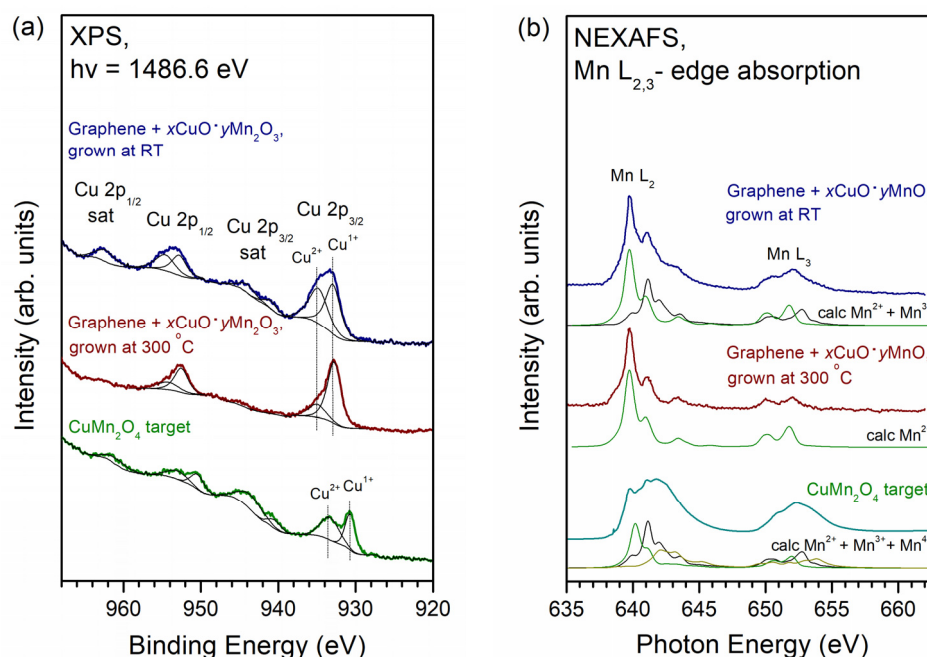

Figure 4. (**a**) Cu 2p XPS spectra; (**b**) Mn 2p NEXAFS spectra of pulsed-laser deposited functionalizing oxide layers on graphene and the nominally hopcalite target.

The Cu 2p XPS and NEXAFS spectra of samples deposited on Gr at the RT and 300 °C are demonstrated in the left panel of Figure 4. The Cu $2p_{3/2}$ PE spectrum of the RT sample consists of two PE lines at 932.9 eV and 934.8 eV flanked by satellites (denoted as "sat" in figure). The Cu $2p_{3/2}$ PE spectrum of the sample deposited at 300 °C had two similar PE lines at 932.8 eV and 934.9 eV; however, the satellite was barely observable. The observed PE lines are close to Cu^+ (933.4 eV) and Cu^{2+} (934.8 eV) for compounds not of a spinel structure, such as oxides Cu_2O (933.5 eV) and CuO (933.8 eV) [31]. On the surface, the Cu^{2+} can be partially hydroxylated as $Cu(OH)_2$ (934.4 eV) [31]. From XPS, the presence of the $CuMn_2O_4$ phase was not detected in deposited layers on Gr, according to the chemical shift. It can be concluded from Figure 4a that the film deposited at RT had the Cu^+/Cu^{2+} ratio of about 1:1, while in the sample deposited at 300 °C, Cu^+ prevailed with a ratio of about 4:1.

The Mn 2p PE spectra of samples were complex and difficult to analyze due to the multiplet structure [32]. We used NEXAFS and simulations to study the Mn L edge (Figure 4b, right panel). The fine structure of the X-ray absorption spectrum at the Mn 2p of the sample deposited at 300 °C coincides with octahedral Mn^{2+} (90 ± 10%), which indicates the formation of MnO in the cubic crystal structure [30]. For the sample deposited at RT, however, deviation from the Mn^{2+} spectrum appears at the higher energy sides of the L_3 regions of the spectrum. According to the literature [30] and calculations, this indicates Mn^{3+} content. Based on the NEXAFS analysis, Mn exists as a mixture of Mn^{2+} (70 ± 10%) and Mn^{3+} (30 ± 10%) in the RT-deposited sample.

The composition of the layer deposited at 300 °C, containing Cu_2O and CuO in a 4:1 ratio and 90% Mn^{2+}, indicates a further loss of oxygen during PLD in a 0.1 bar N_2 atmosphere. Therefore, the MOX composition deposited on Gr deviated from the initial PLD target and will be denoted as $xCu_2O \cdot yMnO$.

3. Results and Discussion

3.1. Sensor Properties of Pristine Gr/Gas Interface

The sudden jump in the analyte gas concentration initiates a current change through the Gr part of the sensor setup, which is measured as a function of time. After switching off the toxic gas, the recovery kinetics were recorded, but this is not extensively discussed in this work. Sensor response *S* is defined as a relative change in conductance *G*:

$$S = (G - G_0)/G_0, \tag{1}$$

where G_0 is conductance in synthetic air before the introduction of the target gas.

The time dependence was run in an interval between 10^1 and 10^{3-5} s under three measurement regimes: either at RT with 365 nm UV illumination, to speed up the otherwise slow equilibration and recovery times, or at elevated *T* (100 and 150 °C) without exposure to UV light.

Most response curves, although extremely nonexponential, are reasonably well approximated to a sum of two exponentials:

$$G(t) = G_0 + A_1 \left[1 - e^{\frac{-(t-t_0)}{t_1}} \right] + A_2 \left[1 - e^{\frac{-(t-t_0)}{t_2}} \right] \tag{2}$$

In Equation (2), G_0 is the initial conductance and $G(t)$ is conductance at time *t*; t_0 is the initial moment of time, when the respective stepwise change in gas composition was introduced. The time-independent coefficients A_1 and A_2 are amplitudes of conductance change. Total response amplitudes, equal to $A_1 + A_2$, determined by fitting response curves to Equation (2), are depicted for pristine and functionalized graphene sensors in Figure 5. Characteristic times t_1 and t_2 can be interpreted as inverse first-order rate constants for the adsorption or desorption kinetics of gas molecules only in the most simple cases. The sensor speed and reversibility parameters, and the sensitivity and the limit of detection can be qualitatively assessed using Figures 6, 7, and S1–S4. The numerical values of signal formation and recovery time constants are skipped. The complete fitting of time traces has little meaning until a kinetic model is built for the underlying processes that, in turn, would require a special investigation using inert atmospheres, etc. Instead, we focused on achieving partial selectivity and stability/reproducibility of the sensor elements, which is indispensable in e-nose assemblies.

Under different measurement conditions—with UV at RT and at elevated *T* of 100 and 150 °C—the relative responses to all test gases increased considerably for functionalized Gr sensors, as compared to those with pristine CVD Gr (Figure 5). For example, for 300 ppb of O_3 at RT + UV light, large responses occurred for both pristine and functionalized Gr, showing an increase by a factor of 10, from 5% to 51%, in case of $xCu_2O \cdot yMnO$ decoration. Reducing gases at 25 ppm showed no detectable response on pristine Gr when tested with NH_3 and H_2S at 100 and 150 °C, while the functionalized sensors displayed a moderate response to NH_3 (−5.4% at 100 °C) and a strong one to H_2S (−27% at 100 °C).

Both pristine and functionalized Gr samples showed a p-type response, since the conductance increased under electron (e^-) withdrawing gases NO_2 and O_3, as result of the down-shift of the Fermi level in Gr. The conductance diminished in contact with e^- releasing NH_3 and H_2S (Figure 5), in accordance with diminishing the concentration of holes and the up-shift of the Fermi level. The CVD Gr primarily exhibited hole conductivity under ambient conditions, assigned to "chemical doping" by adsorbed O_2 and H_2O [33,34], with the possible contribution of acidic $\equiv$Si–O–H groups of the silica support. Therefore, the opposite response signs towards the oxidizing gases NO_2 and O_3, and the reducing gases NH_3 and H_2S, correspond to a p-type sensor, as expected.
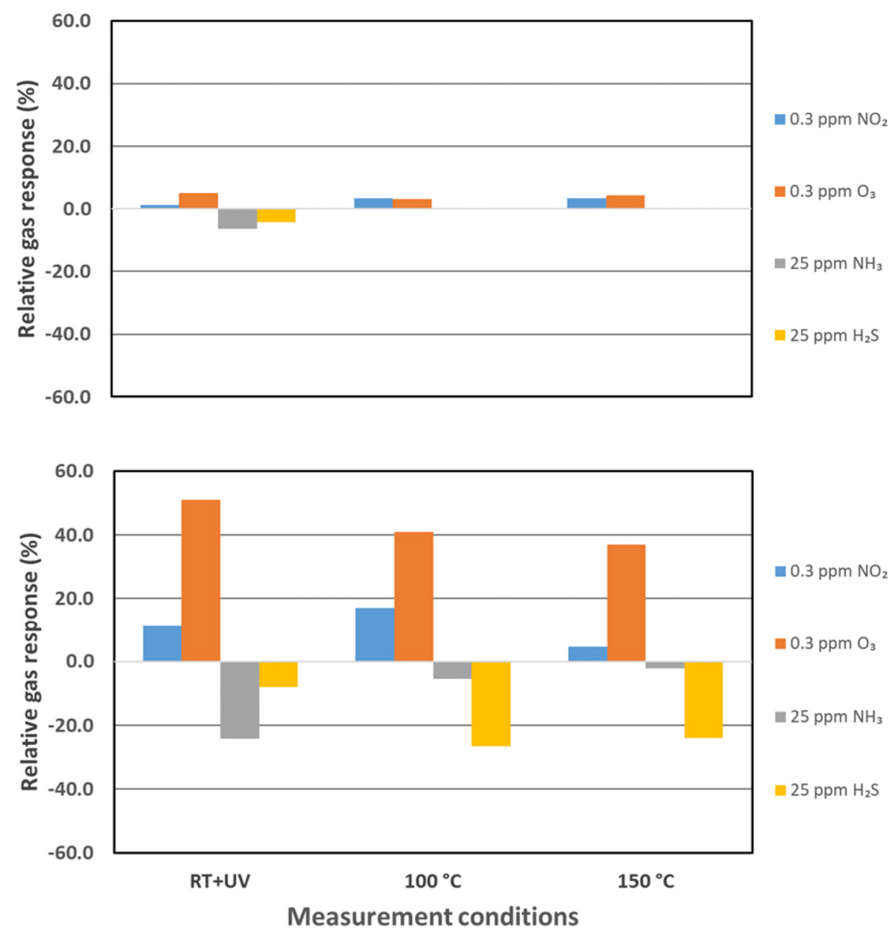
Figure 5. Comparison of conductive responses to small concentrations of poisonous gases on pristine (**top panel**) and functionalized (xCu$_2$O·yMnO grown at 300 °C, **bottom panel**) graphene sensors. Responses were measured at different conditions shown at x-axis. Reducing gases NH$_3$ and H$_2$S at 25 ppm have no detectable response on pristine Gr at 100 and 150 °C.
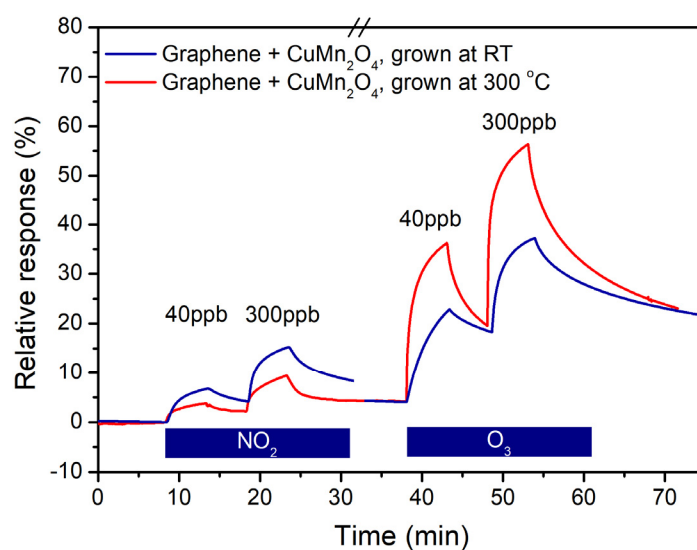

Figure 6. Conductive responses of graphene functionalized with xCu$_2$O·yMnO, deposited at 25 °C and 300 °C, towards NO$_2$ and O$_3$, measured at room temperature under 360 nm UV light excitation. For each analyte, sensor elements are exposed to two consecutive gas pulses lasting 5 min at the concentrations indicated. The peaks of "sawteeth" mark the termination of a gas pulse, followed by relaxation in synthetic air.
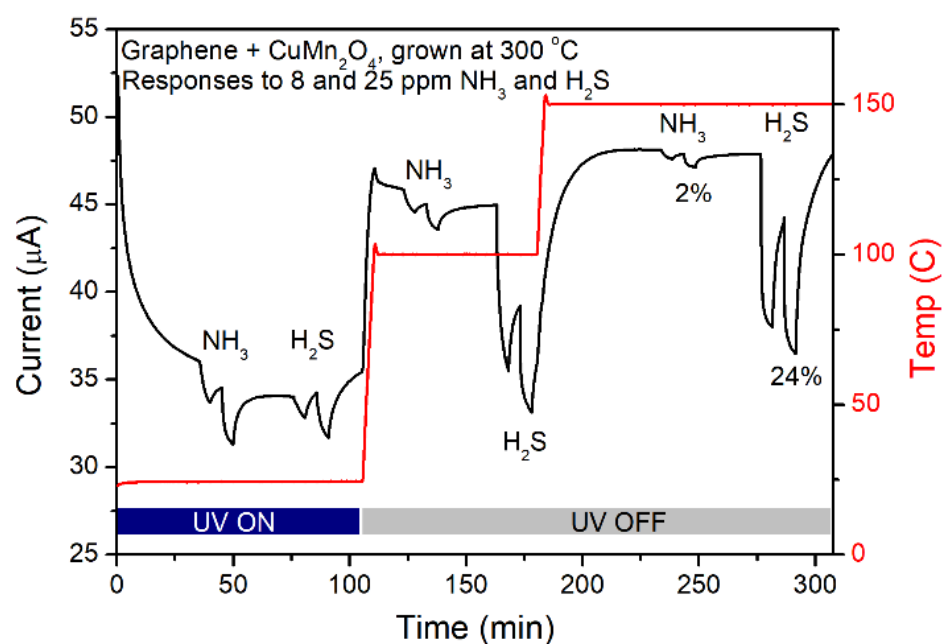
Figure 7. Conductive responses to NH_3 and H_2S of graphene functionalized with $xCu_2O \cdot yMnO$ deposited at 300 °C. Consecutive measurement started at RT with UV light excitation and continued at 100 and 150 °C without light. Red trace/right scale indicate temperature.

At the RT, the conductance of unmodified Gr decreased considerably, by 5–7% under 25 ppm of NH_3, and the signal rise and decay occurred quite fast, i.e., within minutes (Figures 5 and S3). The Gr was quite strongly p-doped and its gas sorption properties were affected by continuous exposure to UV light ($h\nu$). Although NH_3 has an ionization potential IP of 10.07 eV [20], it may fill the hole (h^+) in Gr in a (photoinduced) process, when there is an additional gain in energy, e.g., due to proton release and its hydration with abundantly available water:

$$NH_3 + h^+ + H_2O + [h\nu] \rightarrow \cdot NH_2 + H_3O^+ \qquad (3)$$
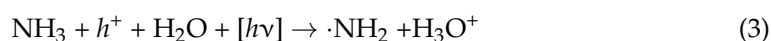
The amino radical and its dimerization product hydrazine would react with holes more easily than NH_3 [35], thus suppressing Gr conductance further and releasing more protons:

$$2 \cdot NH_2 \rightarrow H_2N\text{-}NH_2 \rightarrow HN = NH \rightarrow N \equiv N\uparrow \qquad (4)$$

Probably, the superoxide anion finally serves as a scavenger of protons [35]:

$$H^+ + \cdot O_2^- \rightarrow \cdot HO_2 \rightarrow H_2O + O_2 \qquad (5)$$
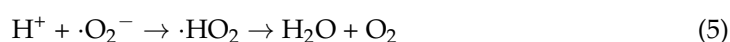
From the viewpoint of practical sensorics, the systems containing neat Gr, being inferior to functionalized Gr, can hardly serve as a reference. Scrutiny concerning several questions of fundamental interest, including the validity of this reaction scheme, the participation of oxygen species, the role of possible defects, impurities, dopants, and edges of Gr, was postponed, since the sensor system remains insufficiently characterized. We confirm what is reported in the literature data that NH_3 desorption is sluggish [36], and the sensor would not reset at RT without UV light. Kinetic traces for a relative conductance change of even smaller magnitude (several %) have been reported for 20–100 ppm of NH_3 at RT and 100 °C, without light, with better results for mica/Gr, as compared to $Si/SiO_2/Gr$ [37].

Absorption of light quanta can either create or destroy electron-hole pairs, and similarly, cause desorption or promote adsorption. In the $Si/SiO_2/Gr$, the conductance fell by ~10% (Supporting Information Figures S1 and S3) as a result of the decreasing hole

concentration, due to h^+-e^- recombination (the latter being probably in the form of $\cdot O_2^-$) and desorption of O_2 [34,38,39]. In the case of MOX decoration, the light effect was even larger (20–30%, Figures 7 and S4). Exposure to light also improved the response rate, and in particular, the recovery time, occasionally at the expense of signal amplitude.

A perfect Gr sheet is a relatively inert material regarding chemisorption, because of lack of suitable adsorption sites, such as dangling bonds, charged atoms, etc. [4,5]. Pristine Gr samples often contain unknown dopant impurities, point defects, punctures, and organic residues left from polymer film used for Gr transfer. Some of these impurities and defects may even be favorable, considering the sensing properties, by providing adsorption sites for small gas molecules. Therefore, typical pristine CVD Gr has some gas sensitivity, usually with slow recovery at RT, referring to the presence of high-affinity adsorption sites present at a low density [5]. A substantial increase in the gas sensitivity of single layer Gr-based sensors is possible by functionalization with defects [5], single dopant atoms [4], and nanostructured thin metal [40] or metal oxide films [7–12].

The substantial increase in the D peak in the Raman spectra (Figure 3) indicates the considerable growth of the defect density in the course of the PLD process. During the PLD of ZrO_2 and metallic Ag, a similar change in the Raman spectra was observed, in parallel with the diminishing electric conductance of Gr, which is explained in terms of the destruction of the 2D lattice of Gr under bombardment with high-energy plasma species [7]. In practice, the loss of Gr conductance in the course of deposition requires a careful optimization of the number and energy of laser pulses, the nature and pressure of buffer gas in the reactor, etc.

It may seem that an increasing number of Gr point defects can even play a positive role in boosting the sensor properties by creating additional adsorption sites. Competition of two very different kinds of binding sites—the Gr defects and the deposited MOX surfaces— is definitely unfavorable from the point of view of the optimization of sensor behavior. When the MOX coverage is dense, the Gr surface, including the defects, would not be accessible to gas molecules. On the other hand, the Gr defect density, as indicated by the Raman spectra, may arise from carbon–oxygen and even carbon–metal chemical bonds (i.e., carbides) with MOX, which should facilitate the e^- exchange rate through the Gr–MOX interface. In our samples, large areas of Gr were bare or very thinly covered with MOX (<1 nm), since the C 1s photoemission line of sp^2-graphene at 284.6 eV in XPS is very strong (not shown). Achieving a thin and uniform coverage of Gr with materials with well-defined receptor properties remains a challenge. In the samples manufactured in this work, the improved sensitivity arose from the increased density of energetically favorable adsorption sites, created by the addition of MOX material on top of Gr, but the contribution of the added defects in the Gr crystal lattice remains unknown.

Remarkably, the conductance of intact single layer Gr acquires sensitivity to large, atmospheric concentrations of O_2 (2–100%) under exposure to 10–20 mWcm^{-2} of 300 nm or 365 nm light [39]. Moreover, with UV illumination, the functionalized Gr is able to detect toxic gases at very low concentrations and operate reversibly as a chemiresistive sensor material at RT [7–12]. First regarded as an alternative to a higher working T of a sensor, UV light was shown to increase the response and speed up the recovery of Gr-based gas sensors [38,39]. The UV light can clean the surface of passivating molecules, such as H_2O and O_2, as a result of photo-induced desorption processes. The UV light also improves sensor recovery times by increasing the desorption rate of target gas molecules or products of their transformation. The benefits of UV excitation in PLD-functionalized Gr sensors working at RT have been observed for Ag, ZrO_2 [7], and V_2O_5 [8–11] as functionalizing layers, for NO_2 and NH_3 as gases, respectively. We admit that excitons created in the MOX phase are most important in photoinduced processes [11], although Gr excitons may contribute, along with localized excitations in molecules (NO_2), reaction products (NO_2^-), or defect centers.

3.2. Processes on Gr/MOX/Gas Interface: Oxidizing Gases

Complete selectivity or specificity has not yet been achieved in Gr-based chemiresistive sensors, at least for small, highly reactive gas molecules in the background of chemically aggressive air [7–12]. This points to a general basic mechanism, and it is assumed that full electron exchange between Gr and its surface is required for producing the conductance changes recorded in our sensor systems. Humid air can promote oxidation reactions and the stabilization of ionic species on polar MOX surfaces, since the concentration of O_2 and H_2O is very high. We will demonstrate that more complex redox mechanisms are likely involved, besides chemisorption by means of e^- transfer.

First of all, the sign of conductance change depends on the direction of e^- transfer. For example, the oxidation of NO_2 to a N^{5+} state (HNO_3, NO_3^-) is possible (e.g., at 150 °C on α-Fe_2O_3 [41]), since NO_2 as a radical species would irreversibly recombine with a hydroxyl radical, if present, to yield nitric acid that is perhaps volatile enough at RT to leave the surface:

$$NO_2 + \cdot OH \rightarrow HNO_3\uparrow \tag{6}$$

However, increasing Gr conductance demonstrates that NO_2 is reduced, rather than oxidized, and e^- is ultimately removed from the already p-doped Gr, thus producing additional holes. The sensor behavior is in accordance with reversible chemisorption of NO_2:

$$NO_2 + e^- \leftrightarrows NO_2^- \tag{7}$$

As electron donors or reducing centers, either metal cations (Mn^{2+}, Cu^+) or oxygen species (O^{2-}, $\cdot O^-$, $\cdot O_2^-$) can play a role [41–44]:

$$NO_2 + M^{n+} \leftrightarrows NO_2^- + M^{n+1} \tag{8}$$

$$NO_2 + \cdot O_2^- \rightarrow NO_2^- + O_2\uparrow \tag{9}$$
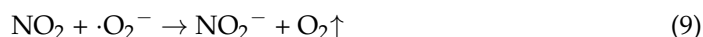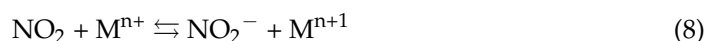
By contrast, ozone decomposition is conceivable without interparticle charge transfer and any noticeable change in Gr conductance. Unexpectedly, the actual sensor response to NO_2 and O_3 was nearly always of comparable magnitude (Figures 5, 6 and S2). The e^- transfer is definitely possible in case of O_3, because of very similar EA for NO_2 (2.273 eV) and O_3 (2.1028 eV) [20]. Consequently, a chemisorption reaction (Equation (7)) also occurs as a primary event for ozone molecules, whereas the p-doped Gr can serve as an ultimate source of e^-:

$$O_3 + e^- \rightarrow \cdot O_3^- \tag{10}$$
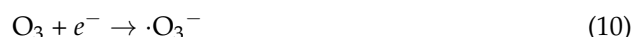
The reaction can take place at a reduced cationic site, for instance:
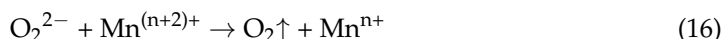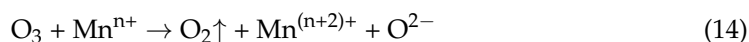
$$O_3 + M^{n+} \rightarrow \cdot O_3^- + M^{(n+1)+} \tag{11}$$
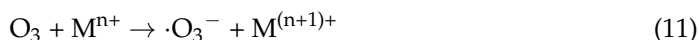
Moreover, it follows from the EA values of O_2 (0.45 eV) and O (1.46 eV) that ozone can also capture an electron from monoanion radicals $\cdot O_2^-$ and $\cdot O^-$. Reaction (11) is probably irreversible, since the ozonide anion radical $\cdot O_3^-$ is very reactive. Still, several alkali ozonides are thermally stable up to ~330 K in dry conditions [42]. Ozonide may not persist on a catalytic MOX surface, and consequently, the chemisorbed ozone is hardly able to leave, prior to dissociating into dioxygen:

$$\cdot O_3^- \rightarrow \cdot O^- + O_2\uparrow \tag{12}$$

As already mentioned, the oxygen monoanion radical $\cdot O^-$ is probably the most stable species on the MOX surface, compared to the parent dianion O^{2-} or O atom [43,44]. Depending on the relative humidity (RH) of the ambient background, protonation of the anion radical $\cdot O_3^-$ followed by splitting is probable [45]:

$$\cdot O_3^- + H^+ \rightarrow OH\cdot + O_2\uparrow \tag{13}$$

In the literature, an oxygen vacancy site is often considered as the most active O_3 decomposition center on the transition MOX surface [46–48]. The two electrons left behind after the O atom is ejected from the lattice will attach to cations, e.g., converting Mn^{4+} into Mn^{2+}. Together with an adjacent void, the latter forms a catalytic center where two ozone decomposition steps can take place one after another [46]:

$$O_3 + Mn^{n+} \rightarrow O_2\uparrow + Mn^{(n+2)+} + O^{2-} \tag{14}$$

$$O_3 + O^{2-} \rightarrow O_2\uparrow + O_2{}^{2-} \tag{15}$$

$$O_2{}^{2-} + Mn^{(n+2)+} \rightarrow O_2\uparrow + Mn^{n+} \tag{16}$$

Reaction (14) includes charge transfer from the metal cation to ozone and reaction (16) shows an active site regeneration step where the O_2 molecule is desorbed, oxygen vacancy is recovered, and the cation is reduced back to its original chemical state. Notice that "oxygen vacancy" is visualized in the course of reactions (14)–(16) as a void that can either be empty, bind one terminus of O_3 or $O_2{}^{2-}$ molecules, or accommodate O^{2-}.

The catalytic decomposition of O_3 also takes place at RT [48] and reaction (16) is possibly the rate-limiting step [47]. Paradoxically, no Gr conductivity response follows from this reaction scheme, since electrons remain localized at the catalytic site. Long-range e^- transport must be assumed between differently charged cations in the lattice, terminating with e^- abstraction from Gr. An alternative pathway of hole diffusion involves the anionic sublattice, beginning from Gr and reaching oxygen vacancy that was cleared of electrons by O_3.

Further, the dianion O^{2-} formed in reaction (14) will probably not wait for the next O_3 molecule to arrive (Equation (15)), which is a rare event at ppb, but react with the abundantly available O_2 to yield superoxide anion radical $\cdot O_2{}^-$. Although documented by Raman spectroscopy at higher O_3 concentrations [49], the peroxide dianion $O_2{}^{2-}$ may not accumulate. Therefore, we are reluctant to consider the two e^- transfers (Equations (14) and (16)) [46] as a main mechanism in our case.

The role of surface oxygen vacancy as an adsorption and reaction site for ozone decomposition is well established [48] and confirmed by DFT calculations for heat-treated MnO_2, including the effect of H_2O [50].

When comparing the responses to 300 ppb NO_2 and O_3 gases, sensors with different deposition *T*s show selectivity towards ozone—by 2.5 and 6.2 times in favor of O_3 for RT-deposited and 300 °C deposited sensors, respectively (measured at RT under UV exposure) (Figure 6).

As for the unexpected selectivity of Gr/MOX sensors towards O_3, in comparison with NO_2, the following possible reasons can be considered:

(1)   Larger charge transfer in the Gr/MOX system may be associated with the irreversible dissociation of O_3, which shuttles two electrons as compared to just one e^- during NO_2 chemisorption;

(2)   The number of suitable adsorption sites on the MOX surface may be smaller for NO_2, as compared to sites for O_3 adsorption.

All in all, the Mn oxides are known as one of the most active groups of oxide catalysts for ozone decomposition [46–48].

It appears that changes in Gr conductance can unravel, with unprecedented sensitivity, with the mechanistic details of the reactions taking place on MOX surfaces being hardly accessible to other methods, including the long-range single electron transfer steps accompanying the O_3 decomposition.

*3.3. Processes on Gr/MOX/Gas Interface: Reducing Gases*

As revealed by sensor responses, reducing gases will release electrons under oxidizing–ionizing conditions on the polar MOX surface exposed to ambient air. Without doubt, the

processes with the participation of NH_3 and H_2S go beyond "elementary" chemisorption and dissociation, and involve irreversible, multi-step oxidations.

In general, if a protic compound such as NH_3 loses e^-, a proton H^+ is liberated immediately and the remaining $\cdot NH_2$ radical can dimerize, forming hydrazine N_2H_4 that spontaneously gives away further electrons and protons, yielding N_2 as a final stable product (Equations (3) and (4)) [51–55]. A probable net reaction scheme summarizing many possible e^- and H^+ transfer pathways is as follows:

$$2NH_3 + 3 \cdot O^- \rightarrow N_2 \uparrow + 3H_2O \uparrow + 3e^- \tag{17}$$
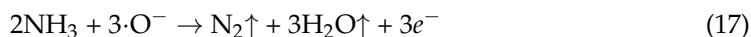
In this reaction, oxidizing cations ($Mn^{3+/4+}$, Cu^{2+}) can serve as binders and carriers of e^-:

$$2NH_3 + 3 \cdot O^- + 3M^{n+} \rightarrow N_2 \uparrow + 3H_2O \uparrow + 3M^{(n-1)+} \tag{18}$$
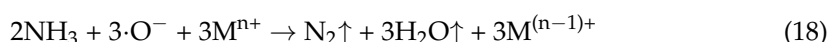
It is known that NH_3 adsorbs strongly on transition metal oxides at Lewis acid sites, located predominantly on coordinatively unsaturated cations nearby oxygen vacancies [51].

"Burning" of a NH_3 molecule is exothermal by -3.29 eV, as calculated from the atomization energies [56]. Strong interactions with adjacent particles in a catalytic site, owing to its electron pair donating and protic character, undoubtedly help to navigate a reaction path with barriers small enough to overcome them at RT. In studies of the selective catalytic oxidation of ammonia with O_2 and NO on MOX, the oxygen atom $\cdot O \cdot$ appears in most chemical equations, and other intermediates are also depicted as electrically neutral [53–55].

By contrast, the unique sensitivity of Gr conductance reveals elementary e^- transfer steps, and the generally ionic character of reactions on MOX surface. Less reactive $\cdot O^-$ and $\cdot O_2{}^-$ are probably more abundant on the surface at RT [57–59], whereas at a higher T, more reactive oxygen atoms and dianions will appear, the surface will be dehydrated, and the species tend to deprotonate. The first step(s) of the process described by Equation (18) are probably thermally activated [52], with a considerable activation energy, since catalytic oxidation of ammonia is accelerated significantly above the RT on manganese oxides [54] and copper oxides [60].

The Ostwald process of a conversion ("over-oxidation") of NH_3 into nitrogen oxides would require specific catalysts and a higher T [52,53], and is not considered here as plausible.

Increased desorption, by lowering the sensor surface coverage of NH_3, causes a dramatic reduction in the sensor response at 100 and 150 °C, as compared with the response at RT (Figures 5, 7 and S4). A large signal able to recover at RT (at least under UV exposure) in the case of NH_3 may point to reversible chemisorption with participation of Lewis acid-type adsorption sites:

$$NH_3 + \square\, M^{n+} \leftrightarrows H_3N \rightarrow M^{n+} \rightarrow \cdot NH_2 + H^+ + M^{(n-1)+} \tag{19}$$

Notice that the donation of undivided e^- pairs ($>\ddot{O}:$, $\equiv N:$) characterizes both the Brønsted and Lewis bases. Brønsted acid refers to an "active" or "bare" proton bound to electronegative elements (O, N, S), whereas the more general Lewis acid can be any e^- pair accepting species with an orbital vacancy (e.g., $\square Mn^{2+}$).

Remarkably, sensor responses to H_2S are reversible, even at RT (Figures 7 and S4). One can write for cation binding, followed by reduction, by analogy with Equation (19):

$$H_2S + \square M^{n+} \leftrightarrows H_2S \rightarrow M^{n+} \rightarrow HS \cdot + H^+ + M^{(n-1)+} \tag{20}$$
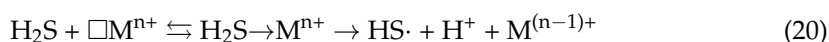
Dimerization of HS· yielding disulfane [61], or rather its reaction products with oxygen species, seems to be able to leave the surface, at least under UV irradiation, assuring fast recovery. Moreover, elementary sulfur as a final product at RT, being inert, may not immediately poison the surface, and the signal remains reversible. There is marked increase
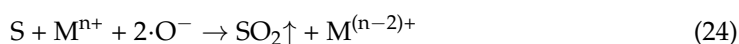
in the sensor response towards H_2S at 100 and 150 °C, compared to response at RT. At higher T, H_2S is easily oxidized to elemental sulfur:
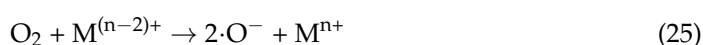
$$H_2S + \cdot O^- \rightarrow S + H_2O\uparrow + e^- \tag{21}$$

or

$$H_2S + \cdot O^- + M^{n+} \rightarrow S + H_2O\uparrow + M^{(n-1)+} \tag{22}$$
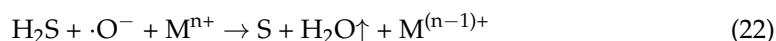
Since the sensor works reversibly and gives a strong signal, conversion to sulfur dioxide is assumed:

$$S + 2 \cdot O^- \rightarrow SO_2\uparrow + 2e^- \tag{23}$$

$$S + M^{n+} + 2 \cdot O^- \rightarrow SO_2\uparrow + M^{(n-2)+} \tag{24}$$

For sensor recovery and active site restoration, the surface reoxidation reaction is plausible:

$$O_2 + M^{(n-2)+} \rightarrow 2 \cdot O^- + M^{n+} \tag{25}$$

The increase in the signal amplitude by about five times between RT and 100 °C points to the enhanced catalytic oxidation of H_2S on the MOX surface to SO_2 (or even SO_3) (Figures 7 and S4).

The hypothetical oxidation reactions of flammable gases on the surface (Equations (21)–(24)) can also be expressed in terms of the participation of dianion O^{2-}, which is, however, less available on the surface at RT (see above), or the superoxide anion radical $\cdot O_2^-$, which is more stable and binds e^- less strongly than $\cdot O^-$ (see the EA values above). In discussions of reducing gases, the term "oxidation" has a double meaning, referring either to e^- transfer or the formation of oxide (i.e., oxygen atom transfer). Table 1 summarizes the MOX–gas interaction mechanisms as discussed in the last two chapters.

Table 1. General adsorption, charge transfer, and reaction mechanisms responsible for sensor signal formation in Gr/MOX/gas system.

Target Gas	Nature of Interaction with Gr/MOX
NO_2	Reversible chemisorption, Equations (7) and (8)
O_3	Chemisorption followed by irreversible catalytic dissociation, Equations (10)–(16)
NH_3	Chemisorption to a Lewis acid site followed by catalytic oxidation to N_2, Equations (17)–(19)
H_2S	Chemisorption at RT and catalytic oxidation in two stages at 100 and 150 °C, Equations (20)–(25)

3.4. Achieving Selectivity of Chemiresistive Gr-Based Gas Sensors

As expected for Gr with hole conductivity, the e^- acceptor gases NO_2 and O_3 increase the conductance (Figures 5, 6, S1 and S2), while the e^- donor gases NH_3 and H_2S reduce the number of carriers and the conductance (Figures 5, 7, 8, S3 and S4). The mutual compensation of signals is a real possibility when oxidizing and flammable gases coexist (e.g., NO_2 and CO in the engine exhaust). Distinct partial selectivity for individual sensor elements would alleviate such cross-talk problems in sensor assemblies ("electronic noses"). Here, we demonstrate a concerted effort in this direction, using variations of MOX deposition conditions, UV light ($h\nu$), and T (k_BT).

It is evident from Figure 5 that the amplitudes of sensor responses tend to diminish with an increasing measurement T. This is particularly strong for NH_3 and, to a smaller extent, for NO_2 and O_3, with H_2S being an exception. The surface T has a stronger effect on desorption phenomena, rather than on adsorption rates, since escaping the potential well needs more activation energy. Consequently, the surface coverage and the sensor response decrease with T at the same target gas concentration. The responses to reducing gases NH_3 and H_2S are of a comparable magnitude, being larger for NH_3 at RT (Figures 5 and 7);

however, at a higher measurement T (100 and 150 °C), a promising selective enhancement towards H_2S appears. Specifically, the sample functionalized at 300 °C has a three times larger response to NH_3 as compared to H_2S at 25 ppm when measured at RT (+UV light), but the ratio is reversed at 100 °C when the signal for H_2S exceeds that for NH_3 by a factor of 5. The responses to NH_3 of both functionalized sensors diminish fast with an increasing T (Figures 5, 7 and S4), due to acceleration of desorption rates reducing both the surface coverage and the sensor response. The T dependence of the H_2S response is drastically different, rising from 8% at RT to 27% at 100 °C and to 24% at 150 °C for a sensor functionalized at 300 °C. The sensor with MOX deposited at RT is similar in terms of the increase in the selectivity towards H_2S at a higher measurement T, but the amplitudes are smaller (Figures 8 and S4).
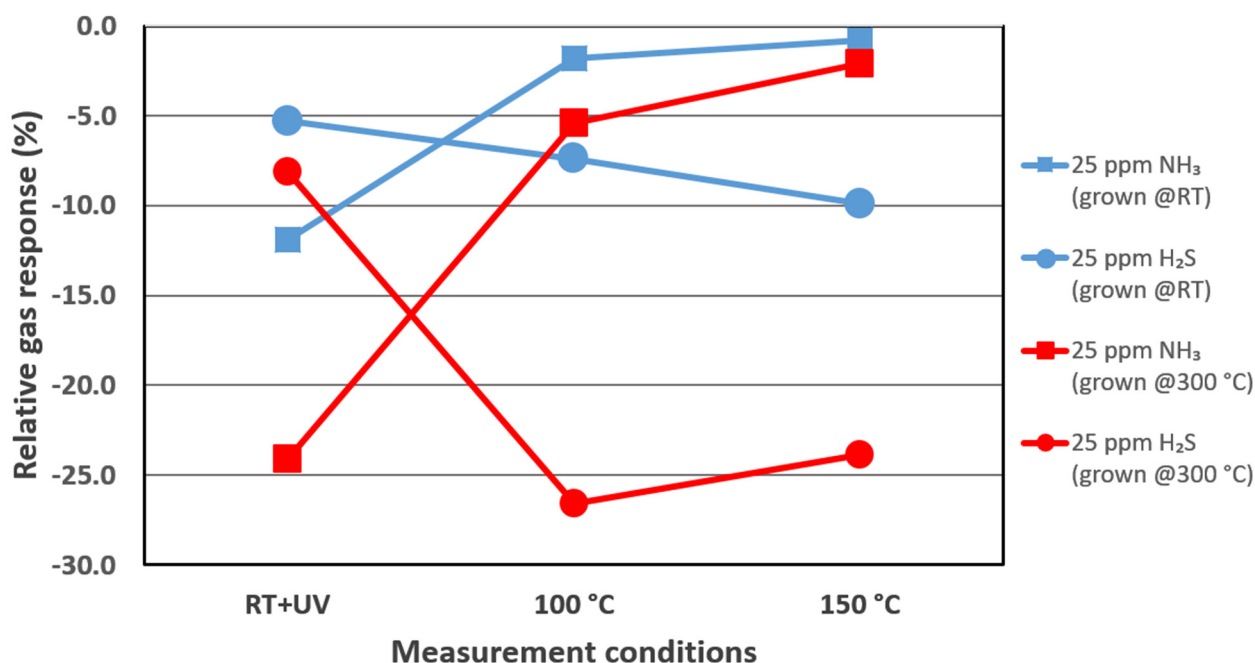

Figure 8. Dependence of relative conductance change on measurement temperature (and the presence of UV light) for reducing toxic gases. The selectivity towards H_2S emerges with rising T (and no UV). Functionalizing xCu$_2$O·yMnO layers were grown by PLD at RT and 300 °C (red lines). Notice that, for the respective gases, red data points indicate invariably larger response magnitude, perhaps pertaining to MOX crystallinity.

The effect of an increased measurement T on sensor performance is somewhat similar to that of UV light. It improves the response towards the target gas, possibly by the desorption of interfering O_2 and H_2O, and speeds up sensor recovery, due to thermally activated desorption. A higher T activates the catalytic processes, e.g., oxidation of gases at the MOX surface, which can result in a considerably increased response and recovery.

Instead of sensor excitation with UV light, raising (or cyclically changing) the working T is the most preferred method for improving the dynamics and/or selectivity of gas sensor elements in practical applications. In addition, it was shown that performing gas measurements at several parallel T or even using dynamic T regimes can be extremely beneficial in terms of discriminating several species in the gas mixtures [62]. The miniature sensor substrates containing many distinct pixels with built-in microheaters are used by commercial producers in state-of-the-art gas sensors.

In contrast to a simple reversible adsorption/desorption cycle of NO_2, the irreversible catalytic reactions with atmospheric O_2 play a predominant role in sensor signal build-up and recovery in the case of flammable gases. On MOX surfaces, different oxygen particles exist and participate in chemical transformations [63–65]. The chemical reactions

on the surface are necessarily catalytic, almost by definition. A reliable connection between catalytic oxidation reactions taking place on activating MOX layers, and the adjoining Gr conductivity was established. A marriage of heterogeneous catalysis and Gr-based conductive sensors appears highly promising, bearing in mind the great importance of redox phenomena on solid surfaces and a large number of chemical transformations studied in detail.

In order to affect the Gr conductance, the e^- release or capture events on MOX surface should change the "doping" of Gr, equivalent to Fermi level shifts. It is proposed that the most common e^-/hole transfer mechanism in MOX, particularly in oxides with a disordered structure, is phonon (eventually photon)-induced diffusion of small polarons between the ions and defects [43]. The e^- exchange between Gr and MOX should be fast enough to keep response times in acceptable limits. Because of the Fermi level shift, the conductivity of Gr will be modulated and the system can work as a gas sensor.

As a method of production of thin films, PLD is remarkably flexible. Besides the laser pulse energy, gas composition, and pressure (to slow down plasma particles) in the reactor, the support/growth T can also be tuned. There is also a possibility to optimize the film properties by using various post-deposition treatments. Unfortunately, Gr is prone to oxidation, so that 300 °C is close to a T limit for MOX deposition, but our attempt using 10 Pa nitrogen as buffer gas was successful at that T. The sensor functionalized at 300 °C constantly showed larger (about two times) relative signals than the sensor made at RT, when considering the NH_3-H_2S gas pair (Figure 8) and O_3 (Figure 6) for all measurement conditions and gas concentrations. When comparing sensor performance, one should keep in mind that the relatively better response for the system grown at 300 °C comes at the expense of damaging Gr with suppressed conductance.

4. Conclusions

Single layer graphene (Gr) sensors were functionalized by the pulsed laser deposition (PLD) method using a ceramic hopcalite $CuMn_2O_4$ pellet as a deposition target. According to the XPS analysis, the resulting layers consisted of mixed oxides $xCu_2O \cdot yMnO$. The deposition T had a distinct effect on the oxidation states of Cu and Mn ions and the morphology/crystallinity of the MOX film, and led to a further improvement of the gas sensitivity for layers grown at 300 °C.

In general:

- There is a dramatic increase in the gas sensitivity by an order of magnitude in single layer CVD graphene after covering with ~3 nm thick films of mixed oxides $xCu_2O \cdot yMnO$;
- NO_2 vs. O_3: functionalized Gr sensors showed a stronger response to O_3 at all measuring temperatures;
- NH_3 vs. H_2S: the gas selectivity of functionalized sensors depended on measuring T—the selectivity shifted strongly towards H_2S at higher T.

Several sensor elements with different relative responses can be joined into arrays to obtain the practically required selectivity for the simultaneous detection of different pollutants. With a wide selection of partially selective, stable, and fast sensor elements at hand, a functional electronic nose can be manufactured, supported by advanced signal processing techniques [12].

Electron transfer between the analyte gas and other reactive species on the surface, derived mostly from ambient O_2 and H_2O, is, in most cases, irreversible, leads to the decomposition or oxidation of gas molecules, and is susceptible to catalytic acceleration. Immense chemical and structural variability of possible catalytic surfaces, particularly MOX, holds great promise for achieving selectivity for a multitude of volatile organic compounds (VOCs) [62], as demonstrated here for the reducing gases NH_3 and H_2S.

Besides the utilitarian value in miniature gas sensors, Gr conductance in the Gr/MOX/gas system can be exploited as a uniquely sensitive experimental method for studying (photo)catalytic processes on MOX surfaces.

Supplementary Materials: The following supporting information can be downloaded at: https://www.mdpi.com/article/10.3390/chemosensors11080460/s1, Figure S1: Conductive responses to NO_2 and O_3 of pristine (not functionalised) graphene sensor. Consecutive measurements at room temperature + UV light excitation, 100 and 150 °C. Measured with synthetic air (79/21% N_2/O_2) and 50% relative humidity background. Red trace/right scale indicate temperature. Figure S2: Conductive responses to NO_2 and O_3 of graphene sensor functionalized with PLD $CuMn_2O_4$ deposited at 300 °C and measured at 100 and 150 °C. Measured with synthetic air (79/21% N_2/O_2) and 50% relative humidity background. Figure S3: Conductive responses to NH_3 and H_2S of pristine (not functionalised) graphene sensor. Consecutive measurements at room temperature + UV light excitation, 100 and 150 °C. Measured with synthetic air (79/21% N_2/O_2) and 50% relative humidity background. Red trace/right scale indicate temperature. Figure S4: Conductive responses to NH_3 and H_2S of graphene sensor functionalized with PLD $CuMn_2O_4$ deposited at RT. Consecutive measurements at room temperature + UV light excitation, 100 and 150 °C. Measured with synthetic air (79/21% N_2/O_2) and 50% relative humidity background. Red trace/right scale indicate temperature.

Author Contributions: Conceptualization, I.R., R.J. and M.K.; methodology, M.K., I.R., R.P. and R.J.; validation, M.K.; formal analysis, M.K. and R.P.; investigation, M.K., R.P., J.K. and T.K.; resources, T.A.; data curation, M.K.; writing—original draft preparation, M.K., R.P. and I.R.; writing—review and editing, M.K., I.R. and R.J.; visualization, T.K., J.K., R.P. and M.K.; supervision, R.J.; project administration, R.J.; funding acquisition, R.J. All authors have read and agreed to the published version of the manuscript.

Institutional Review Board Statement: Not applicable.

Informed Consent Statement: Not applicable.

Data Availability Statement: Data supporting reported results can be found in DataDoi repository managed by University of Tartu Library (https://datadoi.ee/ (accessed on 29 June 2023)).

Conflicts of Interest: The authors declare no conflict of interest.

References

1. Schedin, F.; Geim, A.K.; Morozov, S.V.; Hill, E.W.; Blake, P.; Katsnelson, M.I.; Novoselov, K.S. Detection of individual gas molecules adsorbed on graphene. *Nat. Mater.* **2007**, *6*, 652–655. [CrossRef]
2. Ratinac, K.R.; Yang, W.; Ringer, S.P.; Braet, F. Toward ubiquitous environmental gas sensors—Capitalizing on the promise of graphene. *Environ. Sci. Technol.* **2010**, *44*, 1167–1176. [CrossRef] [PubMed]
3. Kong, L.; Enders, A.; Rahman, T.S.; Dowben, P.A. Molecular adsorption on graphene. *J. Phys. Condens. Matter* **2014**, *26*, 443001. [CrossRef] [PubMed]
4. Zhang, Y.-H.; Chen, Y.-B.; Zhou, K.-G.; Liu, C.-H.; Zeng, J.; Zhang, H.-L.; Peng, Y. Improving gas sensing properties of graphene by introducing dopants and defects: A first-principles study. *Nanotechnology* **2009**, *20*, 185504. [CrossRef] [PubMed]
5. Lee, G.; Yang, G.; Cho, A.; Han, J.W.; Kim, J. Defect-engineered graphene chemical sensors with ultrahigh sensitivity. *Phys. Chem. Chem. Phys.* **2016**, *18*, 14198–14204. [CrossRef]
6. Chung, M.G.; Kim, D.H.; Lee, H.M.; Kim, T.; Choi, J.H.; Seo, D.K.; Yoo, J.-B.; Hong, S.-H.; Kang, T.J.; Kim, Y.H. Highly sensitive NO_2 gas sensor based on ozone treated graphene. *Sens. Actuators B Chem.* **2012**, *166–167*, 172–176. [CrossRef]
7. Kodu, M.; Berholts, A.; Kahro, T.; Avarmaa, T.; Kasikov, A.; Niilisk, A.; Alles, H.; Jaaniso, R. Highly sensitive NO_2 sensors by pulsed laser deposition on graphene. *Appl. Phys. Lett.* **2016**, *109*, 113108. [CrossRef]
8. Kodu, M.; Berholts, A.; Kahro, T.; Kook, M.; Ritslaid, P.; Seemen, H.; Avarmaa, T.; Alles, H.; Jaaniso, R. Graphene functionalised by laser-ablated V_2O_5 for a highly sensitive NH_3 sensor. *Beilstein J. Nanotechnol.* **2017**, *8*, 571–578. [CrossRef]
9. Kodu, M.; Berholts, A.; Kahro, T.; Eriksson, J.; Yakimova, R.; Avarmaa, T.; Renge, I.; Alles, H.; Jaaniso, R. Highly sensitive NH_3 sensors using CVD and epitaxial graphene functionalised with vanadium(V) oxide: A comparative study. *Proceedings* **2018**, *2*, 854. [CrossRef]

10. Kodu, M.; Berholts, A.; Kahro, T.; Eriksson, J.; Yakimova, R.; Avarmaa, T.; Renge, I.; Alles, H.; Jaaniso, R. Graphene-based ammonia sensors functionalised with sub-monolayer V_2O_5: A comparative study of chemical vapour deposited and epitaxial graphene. *Sensors* **2019**, *19*, 951. [CrossRef]

11. Rodner, M.; Icardi, A.; Kodu, M.; Jaaniso, R.; Schütze, A.; Eriksson, J. Metal oxide nanolayer-decorated epitaxial graphene: A gas sensor study. *Nanomaterials* **2020**, *10*, 2168. [CrossRef]

12. Lind, M.; Kiisk, V.; Kodu, M.; Kahro, T.; Renge, I.; Avarmaa, T.; Makaram, T.; Zurutuza, A.; Jaaniso, R. Semiquantitative classification of two oxidizing gases with graphene-based gas sensors. *Chemosensors* **2022**, *10*, 68. [CrossRef]

13. Lamb, A.B.; Bray, W.C.; Frazer, J.C.W. The removal of carbon monoxide from air. *J. Ind. Eng. Chem.* **1920**, *12*, 213–221. [CrossRef]

14. Lamb, A.B.; Scalione, C.C.; Edgar, G. The preferential catalytic combustion of carbon monoxide in hydrogen. *J. Am. Chem. Soc.* **1922**, *44*, 738–757. [CrossRef]

15. Dollimore, D.; Tonge, K.H. The constitution and oxidizing properties of materials in the copper(II) oxide-manganese(III) oxide system. *J. Chem. Soc. A* **1970**, 1728–1731. [CrossRef]

16. Vepřek, S.; Cocke, D.L.; Kehl, S.; Oswald, H.R. Mechanism of the deactivation of hopcalite catalysts studied by XPS, ISS, and other techniques. *J. Catal.* **1986**, *100*, 250–263. [CrossRef]

17. Schwab, G.-M.; Kanungo, S.B. Die katalytische Verstärkung im Hopcalit. *Z. Phys. Chem.* **1977**, *107*, 109–120. [CrossRef]

18. Dey, S.; Dhal, G.C. Synthesis of hopcalite catalysts by various methods for improved catalytic conversion of carbon monoxide. *Mater. Sci. Energy Technol.* **2020**, *3*, 377–389. [CrossRef]

19. Kótai, L.; Petruševski, V.M.; Bereczki, L.; Béres, K.A. Catalytic properties of the spinel-like $Cu_xMn_{3-x}O_4$ copper manganese oxides—An overview. *Catalysts* **2023**, *13*, 129. [CrossRef]

20. Lide, D.R. (Ed.) *CRC Handbook of Chemistry and Physics*, 89th ed.; CRC Press: Boca Raton, FL, USA, 2008; ISBN 142006679X.

21. Batakliev, T.; Georgiev, V.; Anachkov, M.; Rakovsky, S.; Zaikov, G.E. Ozone decomposition. *Interdiscip. Toxicol.* **2014**, *7*, 47–59. [CrossRef]

22. Korotcenkov, G.; Brinzari, V.; Cho, B.K. In_2O_3- and SnO_2-based thin film ozone sensors: Fundamentals. *J. Sens.* **2016**, *2016*, 3816094. [CrossRef]

23. Wei, P.; Bieringer, M.; Cranswick, L.M.D.; Petric, A. In situ high-temperature X-ray and neutron diffraction of Cu–Mn oxide phases. *J. Mater. Sci.* **2010**, *45*, 1056–1064. [CrossRef]

24. Shoemaker, D.P.; Li, J.; Seshadri, R. Unraveling atomic positions in an oxide spinel with two Jahn-Teller ions: Local structure investigation of $CuMn_2O_4$. *J. Am. Chem. Soc.* **2009**, *131*, 11450–11457. [CrossRef] [PubMed]

25. Fairley, N.; Fernandez, V.; Richard-Plouet, M.; Guillot-Deudon, C.; Walton, J.; Smith, E.; Flahaut, D.; Greiner, M.; Biesinger, M.; Tougaard, S.; et al. Systematic and collaborative approach to problem solving using X-ray photoelectron spectroscopy. *Appl. Surf. Sci. Adv.* **2021**, *5*, 100112. [CrossRef]

26. Pärna, R.; Sankari, R.; Kukk, E.; Nõmmiste, E.; Valden, M.; Lastusaari, M.; Kooser, K.; Kokko, K.; Hirsimäki, M.; Urpelainen, S.; et al. FinEstBeaMS—A wide-range Finnish-Estonian Beamline for Materials Science at the 1.5 GeV storage ring at the MAX IV Laboratory. *Nucl. Instrum. Methods Phys. Res. A* **2017**, *859*, 83–89. [CrossRef]

27. Stavitski, E.; de Groot, F.M.F. The CTM4XAS program for EELS and XAS spectral shape analysis of transition metal L edges. *Micron* **2010**, *41*, 687–694. [CrossRef] [PubMed]

28. Ferrari, A.C.; Meyer, J.C.; Scardaci, V.; Casiraghi, C.; Lazzeri, M.; Mauri, F.; Piscanec, S.; Jiang, D.; Novoselov, K.S.; Roth, S.; et al. Raman spectrum of graphene and graphene layers. *Phys. Rev. Lett.* **2006**, *97*, 187401. [CrossRef]

29. Ferrari, A.C.; Basko, D.M. Raman spectroscopy as a versatile tool for studying the properties of graphene. *Nat. Nanotechnol.* **2013**, *8*, 235–246. [CrossRef]

30. Gilbert, B.; Frazer, B.H.; Belz, A.; Conrad, P.G.; Nealson, K.H.; Haskel, D.; Lang, J.C.; Srajer, G.; Stasio, G.D. Multiple scattering calculations of bonding and X-ray absorption spectroscopy of manganese oxides. *J. Phys. Chem. A* **2003**, *107*, 2839–2847. [CrossRef]

31. McIntyre, N.S.; Cook, M.G. X-ray photoelectron studies on some oxides and hydroxides of cobalt, nickel, and copper. *Anal. Chem.* **1975**, *47*, 2208–2213. [CrossRef]

32. Biesinger, M.C.; Payne, B.P.; Grosvenor, A.P.; Lau, L.W.M.; Gerson, A.R.; Smart, R.S.C. Resolving surface chemical states in XPS analysis of first row transition metals, oxides and hydroxides: Cr, Mn, Fe, Co and Ni. *Appl. Surf. Sci.* **2011**, *257*, 2717–2730. [CrossRef]

33. Ryu, S.; Liu, L.; Berciaud, S.; Yu, Y.-J.; Liu, H.; Kim, P.; Flynn, G.W.; Brus, L.E. Atmospheric oxygen binding and hole doping in deformed graphene on a SiO_2 substrate. *Nano Lett.* **2010**, *10*, 4944–4951. [CrossRef]

34. Yang, Y.; Brenner, K.; Murali, R. The influence of atmosphere on electrical transport in graphene. *Carbon* **2012**, *50*, 1727–1733. [CrossRef]

35. Ramis, G.; Yi, L.; Busca, G.; Turco, M.; Kotur, E.; Willey, R.J. Adsorption, activation, and oxidation of ammonia over SCR catalysts. *J. Catal.* **1995**, *157*, 523–535. [CrossRef]

36. Cadore, A.R.; Mania, E.; Alencar, A.B.; Rezende, N.P.; de Oliveira, S.; Watanabe, K.; Taniguchi, T.; Chacham, H.; Campos, L.C.; Lacerda, R.G. Enhancing the response of NH_3 graphene-sensors by using devices with different graphene-substrate distances. *Sens. Actuators B* **2018**, *266*, 438–446. [CrossRef]

37. Aziza, Z.B.; Zhang, Q.; Baillargeat, D. Graphene/mica based ammonia gas sensors. *Appl. Phys. Lett.* **2014**, *105*, 254102. [CrossRef]

38. Chen, G.; Paronyan, T.M.; Harutyunyan, A.R. Sub-ppt gas detection with pristine graphene. *Appl. Phys. Lett.* **2012**, *101*, 053119. [CrossRef]

39. Berholts, A.; Kahro, T.; Floren, A.; Alles, H.; Jaaniso, R. Photo-activated oxygen sensitivity of graphene at room temperature. *Appl. Phys. Lett.* **2014**, *105*, 163111. [CrossRef]

40. Eriksson, J.; Puglisi, D.; Kang, Y.H.; Yakimova, R.; Spetz, A.L. Adjusting the electronic properties and gas reactivity of epitaxial graphene by thin surface metallization. *Phys. B Condens. Matter* **2014**, *439*, 105–108. [CrossRef]

41. Busca, G.; Lorenzelli, V. Infrared study of the adsorption of nitrogen dioxide, nitric oxide and nitrous oxide on hematite. *J Catal.* **1981**, *72*, 303–313. [CrossRef]

42. Horváth, M.; Bilitzky, L.; Hüttner, J. *Ozone*; Elsevier: Amsterdam, The Netherlands, 1985; p. 294. ISBN 10: 0444996257.

43. Cox, P.A. *Transition Metal Oxides*; Oxford University Press: Oxford, UK, 2010; 296p, ISBN 9780199588947.

44. Henrich, V.E.; Cox, P.A. *The Surface Science of Metal Oxides*; Cambridge University Press: Oxford, UK, 1994; 464p, ISBN 0–521–44389-X. [CrossRef]

45. Pryor, W.A. Mechanisms of radical formation from reactions of ozone with target molecules in the lung. *Free. Radic. Biol. Med.* **1994**, *17*, 451–465. [CrossRef] [PubMed]

46. Radhakrishnan, R.; Oyama, S.T.; Chen, J.G.; Asakura, K. Electron transfer effects in ozone decomposition on supported manganese oxide. *J. Phys. Chem. B* **2001**, *105*, 4245–4253. [CrossRef]

47. Zhang, L.; Wang, S.; Lv, L.; Ding, Y.; Tian, D.; Wang, S. Insights into the reactive and deactivation mechanisms of manganese oxides for ozone elimination: The roles of surface oxygen species. *Langmuir* **2021**, *37*, 1410–1419. [CrossRef] [PubMed]

48. Liu, Y.; Zhang, P. Catalytic decomposition of gaseous ozone over todorokite-type manganese dioxides at room temperature: Effects of cerium modification. *Appl. Catal. A Gen.* **2017**, *530*, 102–110. [CrossRef]

49. Li, W.; Gibbs, G.V.; Oyama, S.T. Mechanism of ozone decomposition on a manganese oxide catalyst. 1. In situ Raman spectroscopy and ab initio molecular orbital calculations. *J. Am. Chem. Soc.* **1998**, *120*, 9041–9046. [CrossRef]

50. Zhu, G.; Zhu, J.; Jiang, W.; Zhang, Z.; Wang, J.; Zhu, Y.; Zhang, Q. Surface oxygen vacancy induced α-MnO_2 nanofiber for highly efficient ozone elimination. *Appl. Catal. B Environ.* **2017**, *209*, 729–737. [CrossRef]

51. Busca, G.; Lietti, L.; Ramis, G.; Berti, F. Chemical and mechanistic aspects of the selective catalytic reduction of NO_x by ammonia over oxide catalysts: A review. *Appl. Catal. B* **1998**, *18*, 1–36. [CrossRef]

52. Ruan, C.; Wang, X.; Wang, C.; Zheng, L.; Li, L.; Lin, J.; Liu, X.; Li, F.; Wang, X. Selective catalytic oxidation of ammonia to nitric oxide via chemical looping. *Nat. Commun.* **2022**, *13*, 718. [CrossRef]

53. Gao, F.; Liu, Y.; Sani, Z.; Tang, X.; Yi, H.; Zhao, S.; Yu, Q.; Zhou, Y. Advances in selective catalytic oxidation of ammonia (NH_3-SCO) to dinitrogen in excess oxygen: A review on typical catalysts, catalytic performances and reaction mechanisms. *J. Environ. Chem. Eng.* **2021**, *9*, 104575. [CrossRef]

54. Kapteijn, F.; Singoredjo, L.; Andreini, A.; Moulijn, J.A. Activity and selectivity of pure manganese oxides in the selective catalytic reduction of nitric oxide with ammonia. *Appl. Catal. B* **1994**, *3*, 173–189. [CrossRef]

55. Xu, L.; Li, X.-S.; Crocker, M.; Zhang, Z.-S.; Zhu, A.-M.; Shi, C. A study of the mechanism of low-temperature SCR of NO with NH_3 on MnO_x/CeO_2. *J. Mol. Catal. A Chem.* **2013**, *378*, 82–90. [CrossRef]

56. Enthalpy of Atomization. Experimental Values. Available online: http://cccbdb.nist.gov/ea1.asp (accessed on 4 July 2023).

57. Batzill, M. Surface science studies of gas sensing materials: SnO_2. *Sensors* **2006**, *6*, 1345–1366. [CrossRef]

58. Chang, S.C. Oxygen chemisorption on tin oxide: Correlation between electrical conductivity and EPR measurements. *J. Vac. Sci. Technol.* **1980**, *17*, 366–369. [CrossRef]

59. Gurlo, A. Interplay between O_2 and SnO_2: Oxygen ionosorption and spectroscopic evidence for adsorbed oxygen. *ChemPhysChem* **2006**, *7*, 2041–2052. [CrossRef] [PubMed]

60. Liang, C.; Li, X.; Qu, Z.; Tade, M.; Liu, S. The role of copper species on Cu/γ-Al_2O_3 catalysts for NH_3-SCO reaction. *Appl. Surf. Sci.* **2012**, *258*, 3738–3743. [CrossRef]

61. Behrend, J.; Winnewisser, G.; Yamada, K.M.T. Synthesis and molecular structure of disulfane. *Z. Naturforsch.* **1991**, *46*, 1338–1342.

62. Schütze, A.; Baur, T.; Leidinger, M.; Reimringer, W.; Jung, R.; Conrad, T.; Sauerwald, T. Highly sensitive and selective VOC sensor systems based on semiconductor gas sensors: How to? *Environments* **2017**, *4*, 20. [CrossRef]

63. Che, M.; Tench, A.J. Characterization and reactivity of molecular oxygen species on oxide surfaces. In *Advances in Catalysis*; Eley, D.D., Pines, H., Weisz, P.B., Eds.; Academic Press: New York, NY, USA, 1983; Volume 32, pp. 1–148. ISSN 03600564. [CrossRef]

64. Diebold, U. The surface science of titanium dioxide. *Surf. Sci. Rep.* **2003**, *48*, 53–229. [CrossRef]

65. Henderson, M.A. A surface science perspective on TiO_2 photocatalysis. *Surf. Sci. Rep.* **2011**, *66*, 185–297. [CrossRef]